catalysts

MDPI

Article

Stable Performance of Supported PdO_x Catalyst on Mesoporous Silica-Alumina of Water Tolerance for Methane Combustion under Wet Conditions

Minseok Kim [1,†], Suhyun Lim [1,†], Chansong Kim [2], Chae-Ho Shin [2], Joon Hyun Baik [3] and Young-Woong Suh [1,4,*]

1 Department of Chemical Engineering, Hanyang University, Seoul 04763, Korea; im.mkim87@gmail.com (M.K.); lim03187@naver.com (S.L.)
2 Department of Chemical Engineering, Chungbuk National University, Cheongju 28644, Korea; cksthd1210@naver.com (C.K.); chshin@chungbuk.ac.kr (C.-H.S.)
3 Department of Chemical and Biological Engineering, Sookmyung Women's University, Seoul 04310, Korea; joonhyun@sookmyung.ac.kr
4 Research Institute of Industrial Science, Hanyang University, Seoul 04763, Korea
* Correspondence: ywsuh@hanyang.ac.kr
† The authors contributed equally to this work.

Abstract: In methane combustion, water tolerance of Pd-based catalysts is quite critical for stable performance, because water is produced in situ and a water-containing feed is used under real conditions. Herein, water-tolerant mesoporous silica-alumina (H-MSA) was prepared by solvent deficient precipitation (SDP) using triethoxy(octyl)silane (TEOOS) and aluminum isopropoxide (AIP). The H-MSA was more tolerant to water than γ-alumina, mesoporous alumina (MA), and mesoporous silica-alumina (MSA) synthesized by using tetraethyl orthosilicate (TEOS), because of the silica present on the external particle surface. Moreover, it exhibited better textural properties, leading to higher dispersion of PdO_x. The PdO_x catalyst supported on H-MSA was quite durable in repeated temperature-programmed cycles and isothermal tests in the presence of water vapor, compared to the reference PdO_x catalysts. The measured stability was attributed to the water tolerance, weak Lewis acidity, and penta-coordinated Al species of the H-MSA support, which was preferentially imparted when TEOOS was added for substitution of 5 mol% AIP for the synthesis of H-MSA. Therefore, the SDP method employed herein is useful in endowing supported PdO_x catalysts with the water tolerance necessary for stable methane combustion performance under wet conditions.

Keywords: methane combustion; solvent-deficient precipitation; mesoporous silica-alumina; supported PdO_x catalyst; water tolerance

Citation: Kim, M.; Lim, S.; Kim, C.; Shin, C.-H.; Baik, J.H.; Suh, Y.-W. Stable Performance of Supported PdO_x Catalyst on Mesoporous Silica-Alumina of Water Tolerance for Methane Combustion under Wet Conditions. *Catalysts* **2021**, *11*, 670. https://doi.org/10.3390/catal11060670

Academic Editors: Marco Torresi, Sergio Camporeale, Vinicio Magi and Francesco Fornarelli

Received: 14 April 2021
Accepted: 22 May 2021
Published: 24 May 2021

1. Introduction

Since methane, a primary component of natural gas and shale gas, has 21 times higher global warming potential than carbon dioxide, it should be gone off by combustion of the gas mixture exhausted after power generation. Among a number of the reported catalyst systems, Pd is mostly known to be the active metal for catalytic methane combustion under oxygen-rich conditions [1–7]. From a number of studies on Pd-based catalysts, the recognized big challenges are complete conversion at temperatures of lower than 400 °C and superior catalyst stability under wet conditions. Particularly, the latter issue is stringent because the water produced by methane combustion ($CH_4 + 2O_2 \rightarrow 2H_2O + CO_2$) and co-feeding water result in catalyst deactivation [8–14]: the surface of PdO is transformed into $Pd(OH)_2$ by the reaction, $PdO + H_2O \rightarrow Pd(OH)_2$, which is favorable below 450 °C [9,13,14]. This leads to blocking of the active PdO_x phase (a mixed state of Pd and PdO) and inhibition of oxygen mobility crucial in the Mars van Krevelen

mechanism [8,9,11–14]. Such deactivation has often been reported in alumina support generally employed for methane combustion [14].

One of the approaches to cope with detrimental effects of water is to provide hydrophobicity to alumina. For instance, Cargnello et al. [15] reported that CeO_2-decorated Pd was deposited onto hydrophobic alumina (H-Al_2O_3) prepared by coating the surface of γ-alumina with triethoxy(octyl)silane (TEOOS), in which the surface of alumina was covered by alkyl chains and hence became hydrophobic. This catalyst showed complete methane conversion at the temperature close to 400 °C in heating cycles. Good water resistance was also demonstrated for Pd on mesostructured Beta zeolite with the optimized hydrophobicity hindering water adsorption [10].

Herein, we have employed a new method different from the coating for the preparation of water-tolerant alumina, which is solvent deficient precipitation (SDP), as described by Woodfield and coworkers [16]. This is a facile, one-pot method and enables the formation of mesopores in the structure of alumina, even after calcination at above 600 °C without use of structure directing agents. Variation in the ratio of water to aluminum alkoxide used in the SDP method affected the rates of hydrolysis and condensation, thereby controlling pore texture of the prepared alumina [17,18]. They also studied the effect of Al substitution by Si, which was performed with addition of tetraethyl orthosilicate (TEOS), on the lattice and coordination environment of mesoporous alumina, and examined improved thermal stability of mesoporous silica-alumina (MSA) because the structure of γ-Al_2O_3 was not transformed into δ- and θ-Al_2O_3 at above 1200 °C by addition of 5 wt% Si to alumina [19].

Thus, TEOS is replaced by TEOOS in this work to provide water tolerance to the SDP-derived mesoporous alumina (MA) prepared by using aluminum isopropoxide ($Al(OC_3H_7)_3$; AIP). The synthesized mesoporous silica-alumina is named H-MSA(*x*) where H represents water tolerance and *x* (5, 10, and 20) is the content of TEOOS added for substitution of 5, 10, and 20 mol% AIP, respectively. For comparison, a series of MSA(*x*) supports are synthesized by using TEOS and AIP, and a commercial γ-Al_2O_3 (gA) is also used. To examine the water tolerance of H-MSA(*x*), the wettability test to measure a contact angle is performed and water-exposed samples are characterized by X-ray diffraction (XRD) analysis. After PdO_x loading, methane combustion activity is evaluated under wet conditions that are chosen referring to the report of Hong et al. [20]. Activity tests are conducted in temperature-programmed and isothermal modes, indicating that PdO_x/H-MSA catalysts are more durable than MSA-supported PdO_x analogues. Thus, the effects of alumina substitution by silica are investigated with respect to acidity and aluminum coordination playing important roles in methane combustion.

2. Results

2.1. Characteristics of the Prepared Supports and Supported PdO_x Catalysts

First of all, H-MSA(10) and MSA(10) were characterized as a representative of the two series of H-MSA and MSA supports to identify water tolerance, respectively. The as-synthesized (i.e., uncalcined) H-MSA(10) was investigated by Fourier-transform infrared (FT-IR) spectroscopy (Figure S1). The absorption peaks in the spectrum were observed at 2900, 2850, and 2875 cm^{-1}, representing the stretching vibrations of the C–H bond of the octyl group [15,21]. They were not found with the samples gA, MA, and MSA(10), but with water-tolerant γ-Al_2O_3 (H-gA) prepared by coating the surface of gA with TEOOS. However, the results of thermogravimetric analysis and elemental analysis revealed that there was no residual carbon species in the calcined H-MSA(10), which is possibly due to calcination at 800 °C.

Thus, the calcined samples were immersed in distilled water for 48 h under ambient conditions to evaluate their water tolerance. Figure 1a shows the X-ray diffraction (XRD) patterns of these water-exposed samples compared to the calcined ones. In the patterns of the calcined gA, MA and MSA(10), the reflections corresponding to γ phase of alumina are visible (black curves). However, when these samples were exposed to water, the new reflections appeared at 2θ of 18.8°, 20.4°, 27.6°, 40.6°, and 53.1° (red curves), which is

because of partial transformation of γ-Al_2O_3 into $Al(OH)_3$ (PDF #20-0011). In contrast, the XRD patterns of both the calcined and water-exposed H-MSA(10) were not noticeably different. This indicates that the exposure of H-MSA(10) to water does not lead to phase transformation unlike the other samples, which corroborates the good tolerance of H-MSA(10) to water.

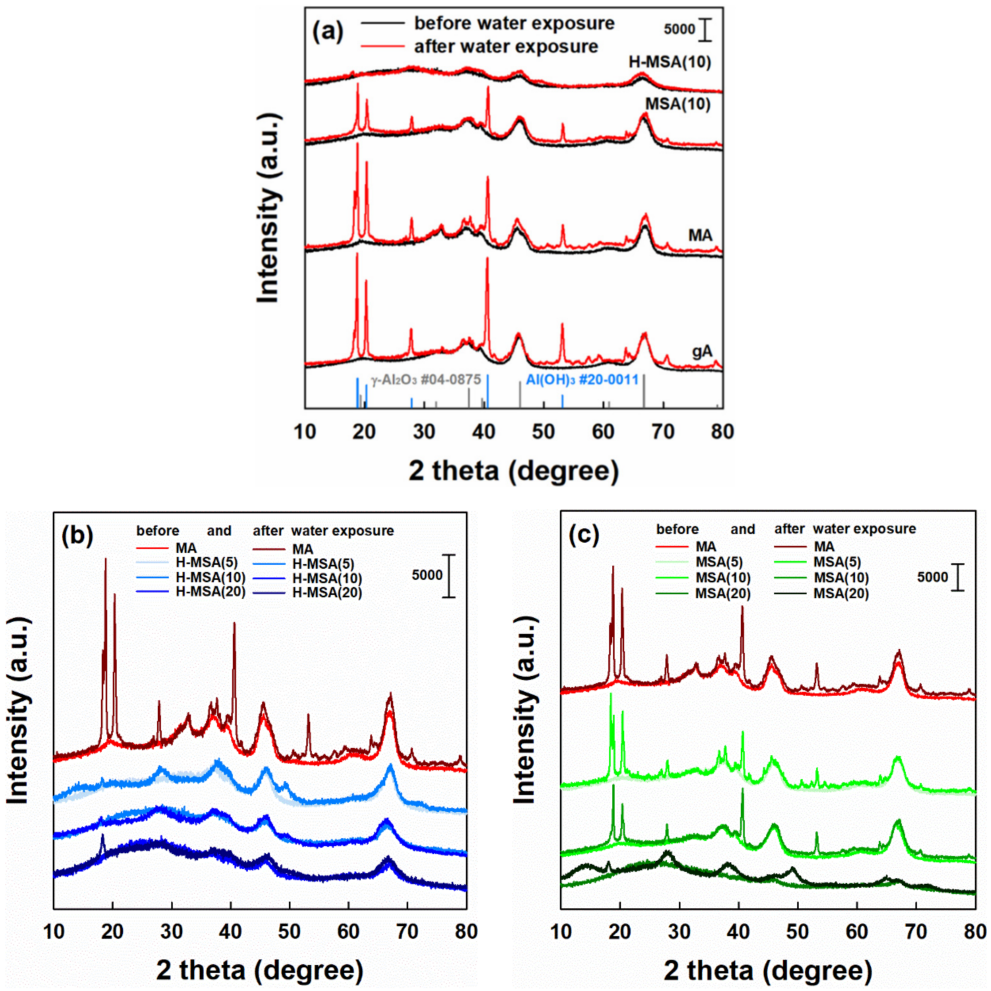

Figure 1. XRD patterns of (**a**) the calcined (black) and water-exposed (red) samples such as H-MSA(10), MSA(10), MA, and gA, (**b**) the calcined and water-exposed H-MSA(*x*), (**c**) the calcined and water-exposed MSA(*x*).

The other water-exposed H-MSA(*x*) and MSA(*x*) samples were further characterized by XRD analysis. Similar to H-MSA(10), H-MSA(5) and H-MSA(20) showed good water tolerance, although the peak at 2θ of 18° was slightly visible for the latter (Figure 1b). In contrast, the diffraction peaks corresponding to $Al(OH)_3$ and AlOOH (boehmite) were detected after the water exposure of MSA(5) and MSA(20), respectively (Figure 1c), where the difference is associated with the amount of TEOS added. Therefore, H-MSA(*x*) is believed to be more tolerant to water than the other prepared supports. Regarding the origin of such a feature, it was noticed that the liquid drops of TEOOS slowly disappeared during the SDP synthesis due to the octyl group, largely different from TEOS showing immediate dissolution. Therefore, the external particle surface of H-MSA(*x*) would be enriched on with silica, which is discussed later. That is, silica enrichment can contribute to the good water tolerance of H-MSA(x).

Additionally, wettability experiments were conducted to measure a contact angle at the pellet surface. Figure S2 shows that the contact angle with H-MSA(10) is higher at

39.1° than 28.0° with MSA(10), 18.7° with gA, and 0° (spreading) with MA. Therefore, it is obvious that H-MSA(10) is more hydrophobic than the other supports. However, H-MSA(10) is not evaluated to be completely hydrophobic because the contact angle is lower than 90°. This suggests that Pd loading is possible by incipient wetness impregnation with an aqueous solution of 10 wt% $4NH_3 \cdot Pd(NO_3)_2$.

Furthermore, spectroscopic study was performed to assess the extent of water uptake for a powder sample. Thus, dry powder samples were taken after pretreatment at 500 °C in a N_2 flow of 40 cm^3 min^{-1} for 1 h, whereas a flow of 50% H_2O in N_2 balance (40 cm^3 min^{-1}) was supplied at 200 °C for 1 h to expose the powder samples to water vapor. After attenuated total reflectance infrared (ATR-IR) spectra of these samples were collected, the spectrum of dry sample was subtracted from that of water vapor-exposed sample. Figure 2 shows the OH stretching and bending vibrations of the adsorbed H_2O in 4000–2700 cm^{-1} and 1800–1500 cm^{-1}, respectively [22]. As clearly seen, the absorptions are very little for H-MSA(10). In other words, the spectra of dry and water vapor-exposed samples are nearly identical, indicating that the water-uptake capacity of H-MSA(10) is negligible. In sharp contrast, MSA(10), MA, and gA exhibit distinct absorption bands in the two regions, which supports that these samples are capable of water uptake. Therefore, the ATR-IR results confirm the good water tolerance of H-MSA(10), as suggested above.

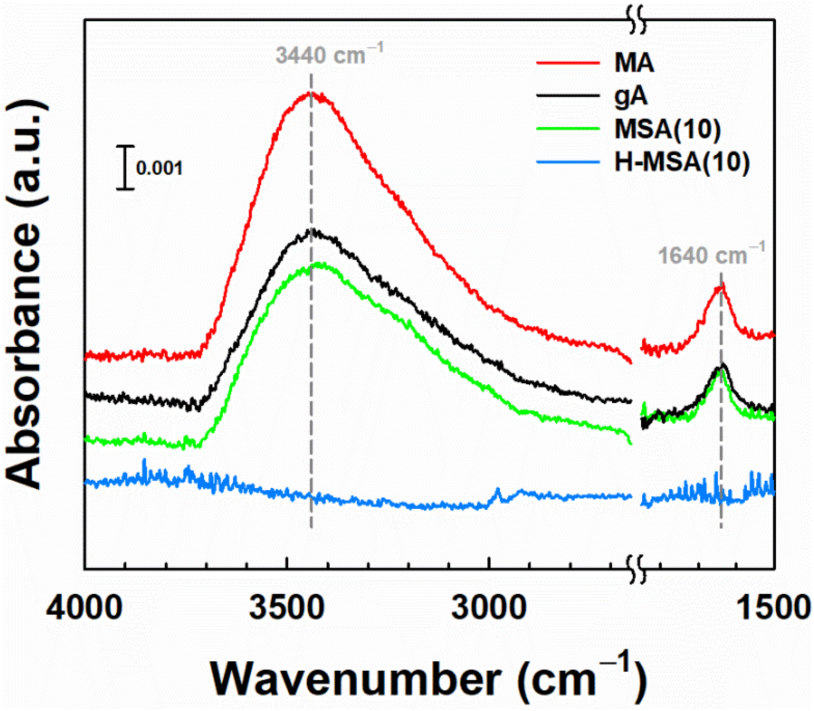

Figure 2. ATR-IR spectra obtained by subtracting the spectrum of dry sample from that of water the vapor-exposed sample. The two regions in 4000–2700 cm^{-1} and 1800–1500 cm^{-1} represent the OH stretching and bending vibrations of the adsorbed H_2O, respectively.

The textural properties of the support materials were characterized by Brunauer-Emmett-Teller (BET) analysis. The measured results are listed in Table 1 and the adsorption-desorption isotherms of supports are presented in Figure S3. When pore size distribution determined by Barrett-Joyner-Halenda (BJH) analysis was plotted against pore width, enlarged mesopores were developed for the MA support centered at 24.2 nm compared to gA of 7.1 nm (Figure S4). This is a feature of the SDP method [16–19]. The pore size distribution curve of MA was similarly observed for MSA(*x*) (Figure 3a). However, the width and height of these curves were reduced with the increase in the amount of TEOS added: 24.1, 19.0, and 11.2 nm for MSA(5), MSA(10), and MSA(20), respectively. This is most likely attributed to the increased rates of hydrolysis and condensation by better mixing

of TEOS and AIP. Thus, the specific BET surface area of MSA(x) decreased from 276 m^2 g^{-1} of MSA(5) to 172 m^2 g^{-1} of MSA(20). In contrast, the H-MSA(x) supports exhibited very broad pore size distribution curves of up to 100 nm (Figure 3b) and the specific surface area also increased from 222 m^2 g^{-1} of H-MSA(5) to 310 m^2 g^{-1} of H-MSA(20) with the center of the pore diameter shifted to a lower value of 14.4 nm. These results would be explained by the presumption that the void space is created by the long hydrocarbon chain of TEOOS acting as a possible spacer between primary alumina particles and preferentially existing at the outer particle surface (explained later by surface composition results).

Table 1. Physicochemical properties of the prepared support materials.

Sample	BET Surface Area [a] (m^2 g^{-1})	Pore Volume [a] (cm^3 g^{-1})	Pore Diameter [b] (nm)	Lewis Acidity [c] (μmol g^{-1})
gA	192	0.44	7.1	59.4
MA	187	1.37	24.2	51.1
MSA(5)	276	1.87	24.1	88.1
MSA(10)	230	1.30	19.0	94.9
MSA(20)	172	0.58	11.2	109.0
H-MSA(5)	222	1.51	34.0	82.4
H-MSA(10)	304	1.45	19.1	69.7
H-MSA(20)	310	1.12	14.4	48.1

[a] Measured by N_2 physisorption at 77 K. [b] Pore diameter when the incremental pore volume was at maximum in pore size distribution curve. [c] Calculated by pyridine-chemisorbed FT-IR spectra.

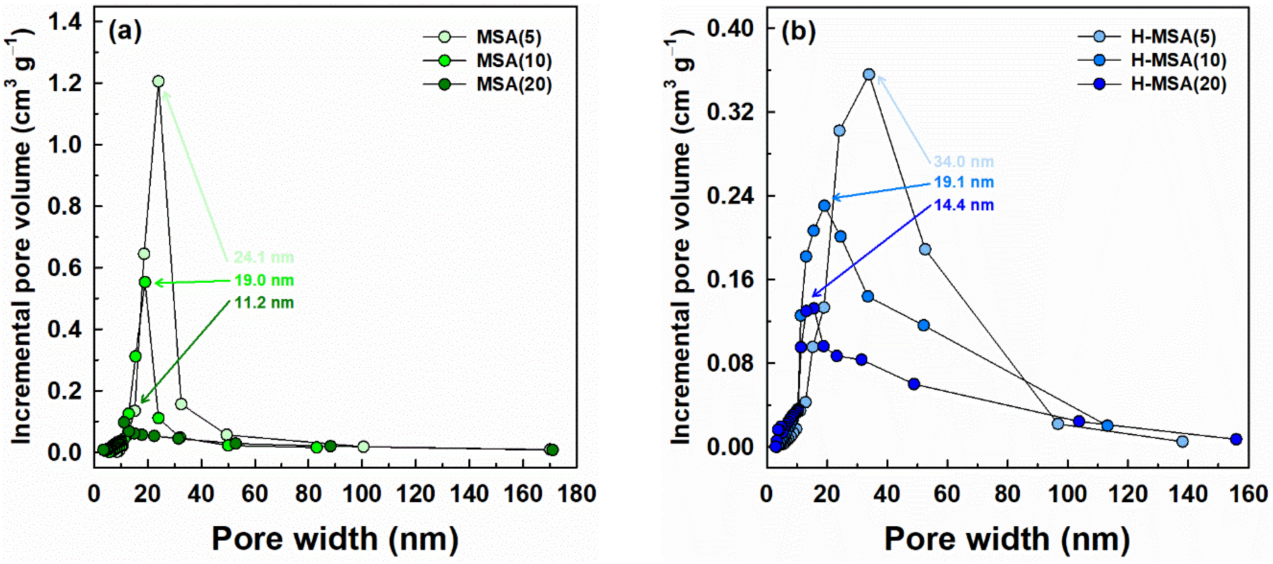

Figure 3. BJH pore size distribution curves of the prepared support materials: (**a**) MSA(x) and (**b**) H-MSA(x).

Additionally, the XRD patterns of the calcined H-MSA(x) and MSA(x) show a background hump in the 2θ range of 10° to 25° (Figure 4). The intensity of this hump became higher with the increase in the amount of TEOOS and TEOS added, resulting from more abundance of amorphous silica. Simultaneously, the reflections of γ-Al_2O_3 became diminished. This may contribute to the change in chemical properties of the alumina surface, aside from the modification of the textural properties discussed above.

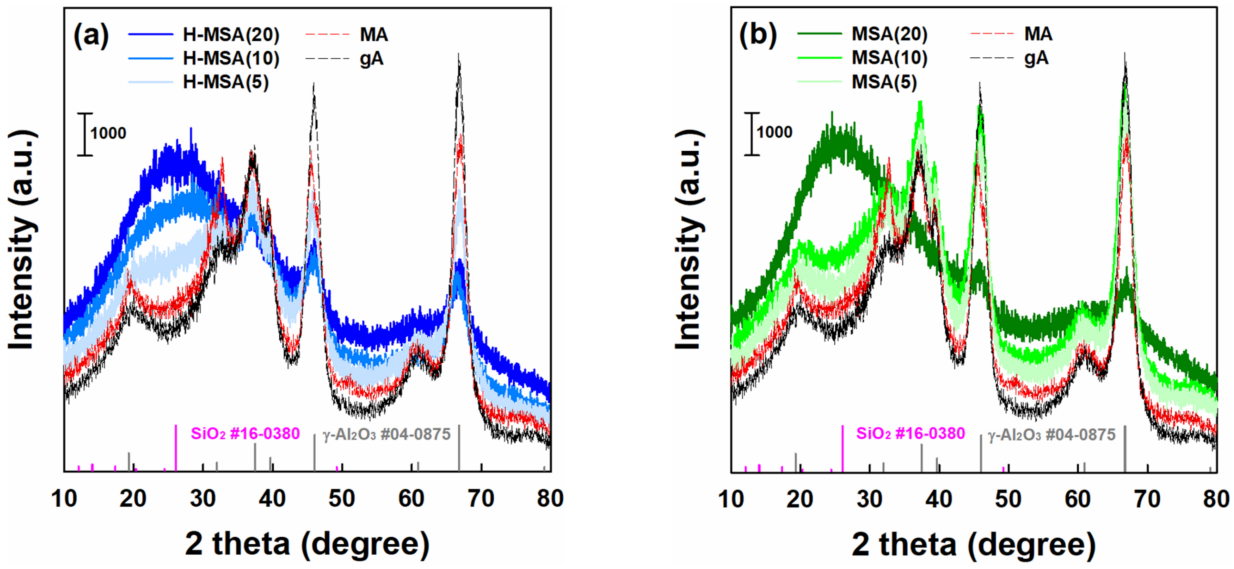

Figure 4. XRD patterns of the calcined support materials, (**a**) H-MSA(*x*) and (**b**) MSA(*x*), along with MA and gA.

CO chemisorption experiments were performed to measure Pd dispersion of the supported PdO_x catalysts (Table 2). Note that the actual Pd content was measured at 2 ± 0.1 wt% for all of the catalysts by an inductively coupled plasma optical emission spectrometer (ICP-OES). The mean value of PdO_x/H-MSA(*x*) was 35.6% (corresponding to Pd size of 3.2 nm), which is much higher than the other catalysts, and is in agreement with the very little reflections of PdO in their XRD patterns. This high Pd dispersion is attributed to the well-developed, broad porosity of H-MSA(*x*) supports. Moreover, H_2 temperature-programmed reduction (H_2-TPR) experiments were performed. Bulk PdO reduces in H_2 at around room temperature, forming Pd hydride species (β-PdH_x). The decomposition of this species shows a negative peak. Generally, the intensity and position of this peak depend on the size of supported Pd particles [23–26]. For instance, the decomposition of β-PdH_x occurs at higher temperatures for small Pd particles while higher storage capacity is observed with larger Pd particles. For the calcined PdO/H-MSA(10), a negative peak was found to be smaller (63.1 μmol g^{-1}) at a higher temperature of 105.5 °C than for PdO/gA, PdO/MA, and PdO/MSA(10) (Figure 5). Therefore, H_2-TPR results confirm the existence of smaller PdO particles on H-MSA(10).

Table 2. Physicochemical properties of the supported PdO_x catalysts.

Sample	BET Surface Area [a] (m^2 g^{-1})	Pore Volume [a] (cm^3 g^{-1})	Pore Diameter [b] (nm)	Pd Dispersion [c] (%)
PdO_x/gA	183	0.42	7.5	29.4 (3.8 nm)
PdO_x/MA	155	0.67	15.5	18.1 (6.2 nm)
PdO_x/MSA(5)	201	0.76	12.9	29.8 (3.7 nm)
PdO_x/MSA(10)	187	0.78	13.9	21.8 (5.1 nm)
PdO_x/MSA(20)	174	0.63	10.0	17.4 (6.4 nm)
PdO_x/H-MSA(5)	217	1.36	20.4	35.2 (3.2 nm)
PdO_x/H-MSA(10)	297	1.23	18.9	34.3 (3.3 nm)
PdO_x/H-MSA(20)	276	0.93	12.9	37.5 (3.0 nm)

[a] Measured by N_2 physisorption at 77 K. [b] Pore diameter when the incremental pore volume was at maximum in pore size distribution curve. [c] Measured by CO chemisorption, where the value in parenthesis indicates the Pd particle size.

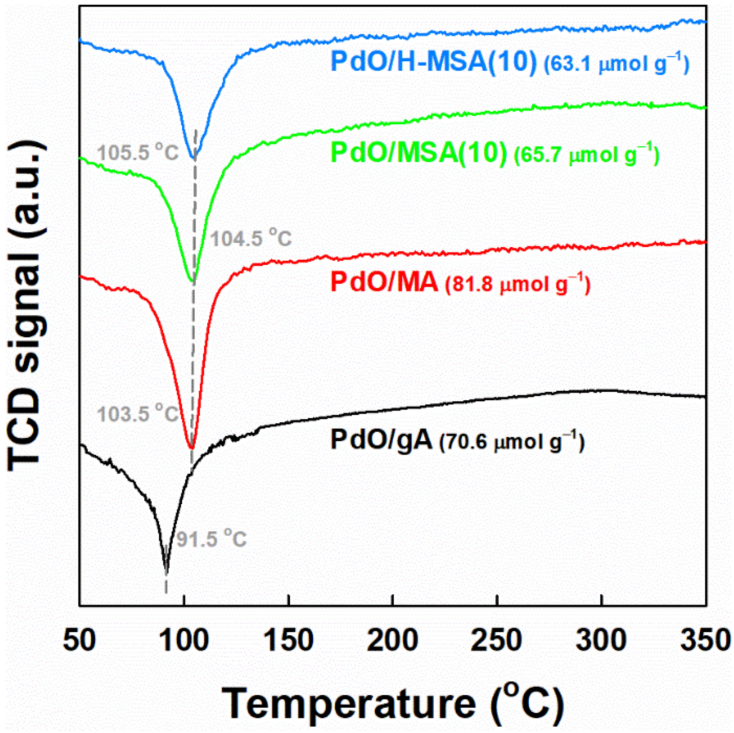

Figure 5. H_2-TPR profiles of the calcined PdO catalysts.

Owing to broad pore size distributions of H-MSA(*x*), palladium precursor species can be infiltrated into enlarged mesopores at the impregnation step and then well dispersed inside pores, which may have more effect on the textural properties of H-MSA(*x*) compared to MSA(*x*). This implication was considered to be valid because the change in the specific surface areas between the supported PdO_x/H-MSA(*x*) catalysts and H-MSA(*x*) was smaller than in between of PdO_x/MSA(*x*) and MSA(*x*). Thus, it can be presumed that sintering of PdO_x is inhibited during methane combustion over PdO_x/H-MSA(*x*) under wet conditions.

2.2. Catalytic Performance in Methane Combustion under Wet Conditions

The methane combustion activities of PdO_x/H-MSA(10) and PdO_x/MSA(10) were first compared through the temperature-programmed test mode in a temperature window of 100 to 600 °C, as presented in Figure 6, where the CH_4 conversion of 90% (T_{90}) was marked by vertical dashed lines. Light-off temperatures were similar at around 300 °C for each catalyst. However, the measured T_{90} was much lower at 385 °C for PdO_x/H-MSA(10) compared to PdO_x/gA (415 °C), PdO_x/MA (430 °C) and PdO_x/MSA(10) (435 °C). This difference is associated with PdO_x size and/or metal-support interaction. Murata et al. reported the metal-support interaction concerning the particle size effect of Pd/Al_2O_3 on methane combustion [27]. When using γ-Al_2O_3 as a support, the catalytic activity decreased with the increase in Pd particle size. This feature was also confirmed in the recent report of Chen et al. [28]. Since the average particle size of Pd in PdO_x/H-MSA(10) was estimated to be 3.3 nm, the size of active PdO_x is considered to positively affect the methane combustion activity of PdO_x/H-MSA(*x*). Nevertheless, metal-support interaction may not be neglected because the difference in Pd particle size was not large among PdO_x/gA, PdO_x/MSA(10), and PdO_x/H-MSA(10).

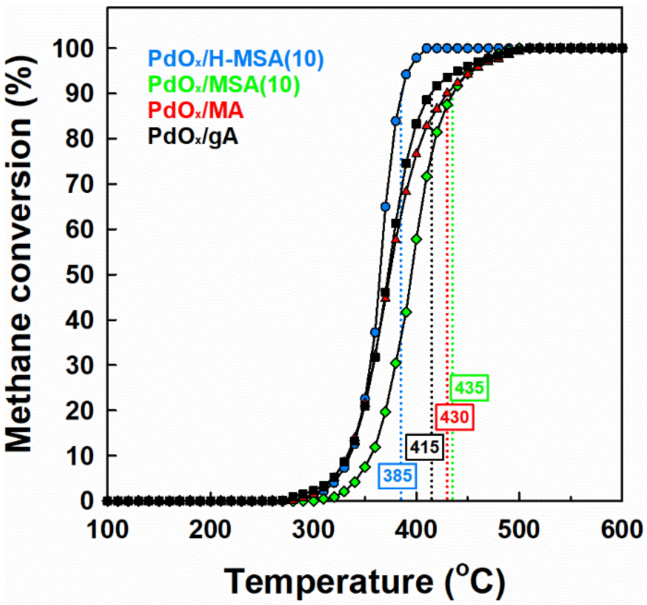

Figure 6. Temperature-programmed methane combustion activities of PdO_x/H-MSA(10), PdO_x/MSA(10), PdO_x/MA and PdO_x/gA from 100 to 600 °C with 4000 ppm CH_4, 12% O_2 and 5% H_2O in N_2 balance (GHSV = 200,000 cm^3 g_{cat}^{-1} h^{-1}). The T_{90} was marked by vertical dashed lines.

To notice activity change resulting from particle sintering and/or change of PdO_x phase, isothermal tests were performed at the activity-favorable temperature, that is, 500 °C. According to the report of Hong et al. [20], 5 vol% of water vapor was contained in the feed with gas hourly space velocity (GHSV). The methane combustion performance of each catalyst was declined at different rates with time-on-stream (Figure 7a). The activity drop was much less for PdO_x/H-MSA(10) (from 99.8% to 88.6%) than for the others such as PdO_x/MSA(10) (from 86.9% to 58.7%), PdO_x/MA (from 88.2% to 43.5%), and PdO_x/gA (from 72.4% to 34.3%). This suggests that the physical and/or chemical state of PdO_x is the most stable in PdO_x/H-MSA(10).

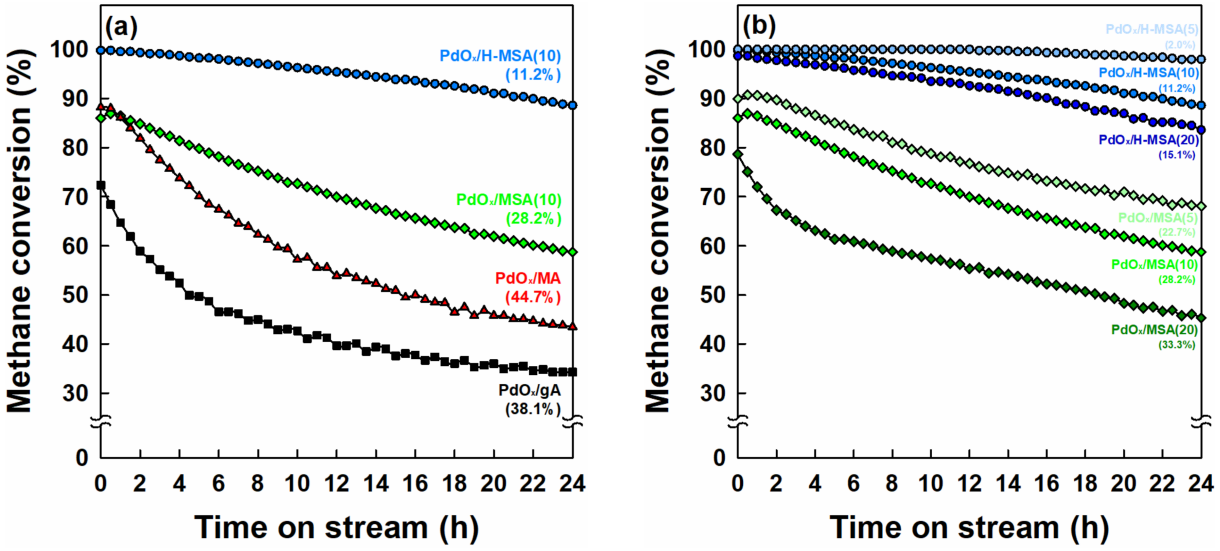

Figure 7. Isothermal methane combustion activities at 500 °C for 24 h with 4000 ppm CH_4, 12% O_2 and 5% H_2O in N_2 balance (GHSV = 200,000 cm^3 g_{cat}^{-1} h^{-1}) over (**a**) supported PdO_x catalysts (PdO_x/H-MSA(10), PdO_x/MSA(10), PdO_x/MSA and PdO_x/gA) and (**b**) the series of PdO_x/H-MSA(x) and PdO_x/MSA(x). The value in parenthesis represents the difference between the initial and final activities.

Furthermore, the catalytic activities of PdO_x/H-MSA(x) and PdO_x/MSA(x) obtained under the same conditions were compared. As presented in Figure 7b, the former catalysts exhibited better stability than the latter. Particularly, the superior performance of PdO_x/H-MSA(5) was maintained at 500 °C for 24 h with a very small decrease from 99.8% to 97.8% compared to PdO_x/H-MSA(10) and PdO_x/H-MSA(20). The degrees of activity decay were much higher for PdO_x/MSA(x): the difference between the initial and final activities was 22.7%, 28.2%, and 33.3% for PdO_x/MSA(5), PdO_x/MSA(10) and PdO_x/MSA(20), respectively.

We tried comparing the activity of PdO_x/H-MSA(5) with the literature data (listed in Table S1). However, it is difficult to make direct comparison because reaction conditions (e.g., CH_4 composition, water content, GHSV, and temperature) are not the same in all reports. Under this situation, GHSV was selected as a reaction parameter for activity comparison because methane conversion strongly depends on the feed flow rate. When our results measured at GHSV of 200,000 $cm^3\ g^{-1}\ h^{-1}$ were compared with the previous results obtained at GHSV of between 180,000 and 240,000 $cm^3\ g^{-1}\ h^{-1}$, the CH_4 conversion (98% at 500 °C) over PdO_x/H-MSA(5) is higher than or comparable to those over PdCe (55% at 450 °C) [29], PdCe SCS (50% at 450 °C) [30], Pd/ZrO_2(85) (95% at 500 °C) [20], and Pd/ZrO_2(700) (85% at 450 °C) [31].

The catalyst stability of PdO_x/H-MSA(x) and PdO_x/MSA(x) was also examined by repeated runs via the temperature-programmed test, where PdO_x/H-MSA(20) and PdO_x/MSA(20) were excluded because of showing the worst activity among their series. When compared with the first-cycle activity curves, the light-off temperatures were almost similar and the T_{90} was shifted to high temperatures with repeated runs (Figure 8). Nevertheless, PdO_x/H-MSA(5) and PdO_x/H-MSA(10) showed the lowest T_{90} values (420–430 °C in the second cycle and 440–450 °C in the third cycle), which is in accordance with the isothermal activity results. In the case of PdO_x/MSA(5) and PdO_x/MSA(10), the T_{90} was measured to be 470 and 490 °C in the second and third cycles, respectively. In contrast, the shift of T_{90} for PdO_x/MA (to 520 °C in the third cycle) and PdO_x/gA (to 530 °C in the third cycle) was much larger, which is also consistent with the significant activity decay observed in the isothermal tests. Therefore, the temperature-programmed test results support the better stability of PdO_x/H-MSA(x).

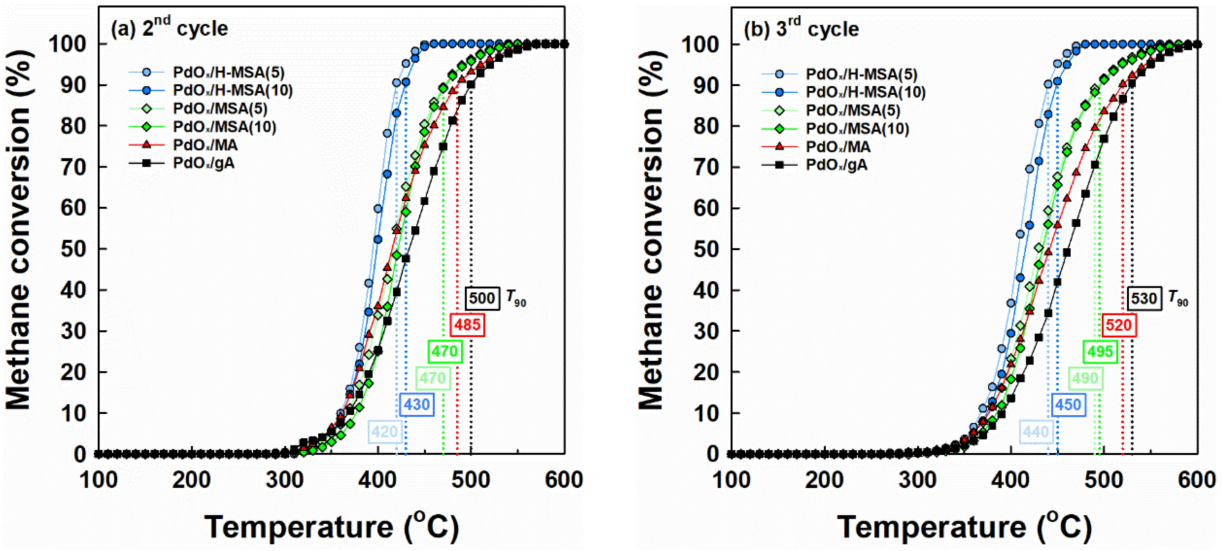

Figure 8. Temperature-programmed activities of PdO_x/H-MSA(5), PdO_x/H-MSA(10), PdO_x/MSA(5), PdO_x/MSA(10), PdO_x/MA and PdO_x/gA in the second (**a**,**b**) third cycles from 100 to 600 °C with 4000 ppm CH_4, 12% O_2 and 5% H_2O in N_2 balance (GHSV = 200,000 $cm^3\ g_{cat}{}^{-1}\ h^{-1}$). The T_{90} was marked by vertical dashed lines.

TEM images of the fresh and spent PdO_x/H-MSA(5) and PdO_x/MSA(5) were shown in Figure 9, where the spent samples were obtained after isothermal test at 500 °C for 24 h

under the conditions stated in Figure 7. The average particle size of PdO_x in the fresh PdO_x/H-MSA(5) and PdO_x/MSA(5) was similar at 3.2 and 3.1 nm, respectively. In the spent samples, the average PdO_x particle size was maintained at 3.3 nm for PdO_x/H-MSA(5), yet the particle growth to 4.7 nm was observed with PdO_x/MSA(10). Similarly, the average PdO_x particle size of PdO_x/H-MSA(10) was negligibly changed after the reaction (fresh: 3.5 nm, spent: 3.8 nm) whereas particle sintering from 3.7 to 4.7 nm was observed for PdO_x/MSA(10) (Figure S5). Similarly, the increase in Pd particle size from 3.6 to 4.9 nm was found with PdO_x/MA (Figure S5). These results clearly explain the better longevity of PdO_x/H-MSA(x) than PdO_x/MSA(x). Additionally, metal-support interaction is considered to be stronger for the former catalysts.

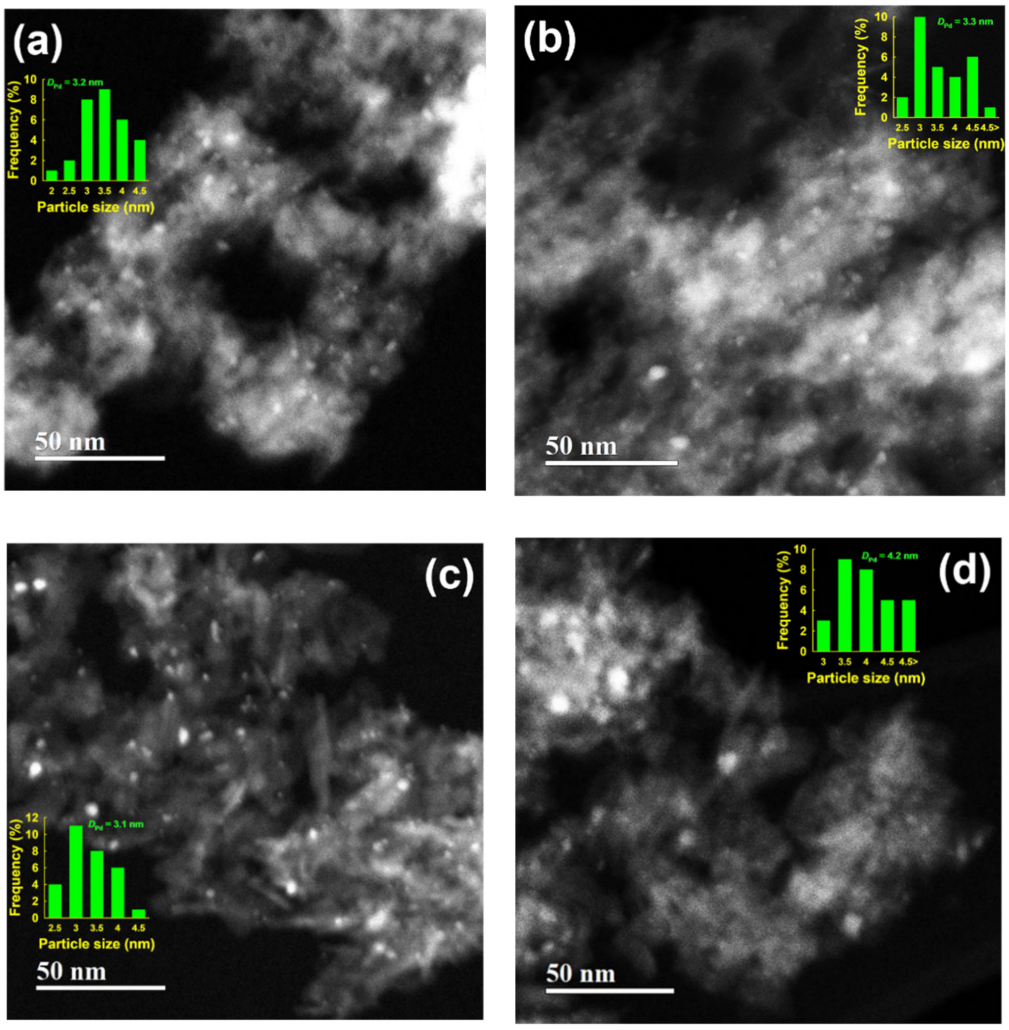

Figure 9. TEM images of (**a**) the fresh PdO_x/H-MSA(5), (**b**) spent PdO_x/H-MSA(5), (**c**) fresh PdO_x/MSA(5), and (**d**) spent PdO_x/MSA(5). The spent samples were obtained after isothermal reaction at 500 °C for 24 h. Insets represent the particle size distribution of PdO_x.

2.3. Effect of Alumina Substitution by Silica

The support materials were characterized to discuss the better long-term stability of PdO_x/H-MSA(x) catalysts. The support acidity was investigated by pyridine-chemisorbed FT-IR spectroscopy (Figure 10), where Lewis acid site was quantified by area calculation of the band at 1450 cm^{-1} with the integrated molar extinction coefficient of 2.22 cm μmol^{-1} [32]. Generally, Pd species become electron deficient by Lewis acidity and thereby result in easy adsorption/desorption of oxygen for methane combustion based on

the Mars van Krevelen mechanism [33]. However, the water has strong affinity to Lewis acidity, possibly leading to catalyst deactivation [10].

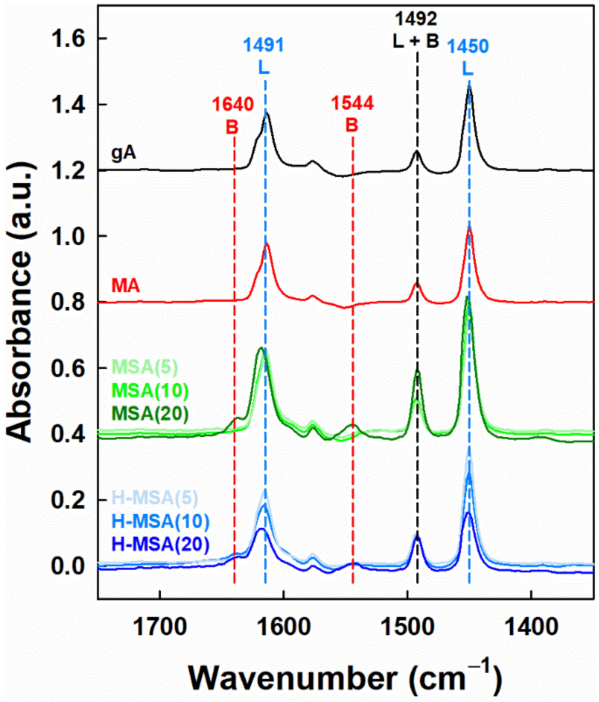

Figure 10. Pyridine chemisorbed FT-IR spectra of the prepared support materials. B and L stands for Brønsted and Lewis acid sites, respectively.

As listed in Table 1, MSA(x) supports were more Lewis acidic than gA and MA due to addition of tetravalent Si into trivalent Al. However, it was reduced for H-MSA(x): 82.4, 69.7, and 48.1 μmol g^{-1} for H-MSA(5), H-MSA(10), and H-MSA(20), respectively. When the surface composition was measured by X-ray photoelectron spectroscopy (XPS), the surface Si content increased in the following trend: 1.9 at% for H-MSA(5) < 3.1 at% for H-MSA(10) < 5.7 at% for H-MSA(20). As shown in Figure S6, the similar trend was observed with MSA(x) but the intensity was lower than those of H-MSA(x): 0.9 at% for MSA(5) < 1.4 at% for MSA(10) < 5.1 at% for MSA(20). This corroborates that Si is enriched at the outer surface of H-MSA(x) compared to MSA(x). Other XPS findings are that the peak of aluminosilicate (centered at 102.3 eV) was predominant in H-MSA(5), and that the surface fraction of SiO_2 (centered at 103.3 eV) was much higher for H-MSA(10) and H-MSA(20). The former explains that most of Si is linked to Al via oxygen atom, implying reduced Lewis acidity of Al for H-MSA(5). The latter observation also suggests that silica present on the external surface can block Lewis acidic Al sites. Therefore, the reduced Lewis acidity of H-MSA(x) with increasing x is likely to inhibit adsorption of oxygen by competitive H_2O adsorption and thereby bring about a little faster catalyst deactivation under wet conditions. On the other hand, the bands at 1544 and 1640 cm^{-1} representing Brønsted acidity were slightly intense for H-MSA(20) and MSA(20) (Figure 10). Because Brønsted acidity with the H-donating ability can hardly cleave C–H bond in CH_4, a low catalytic activity is expected. This matches the lower activities of PdO_x/H-MSA(20) and PdO_x/MSA(20).

In addition, the environment of Al was studied by solid-state ^{27}Al magic angle spinning nuclear magnetic resonance (MAS NMR) spectroscopy. The obtained spectra shown in Figure S7 were deconvoluted into octahedral Al^{VI}, penta-coordinated Al^{V} and tetrahedral Al^{IV} at ca. 8, 31, and 64 ppm, respectively [19,33,34]. The calculated fractions of these species are presented in Figure 11. The fraction of Al^{V} was lower for MA (6.2%) than for gA (14.1%). In addition, it increased to 17.6% and 12.2% for MSA(5) and MSA(10). A further

increase was found with H-MSA(5) (26.4%) and H-MSA(10) (23.9%). Mardkhe et al. [19] reported that the increased concentration of Al^V species in mesoporous silica-alumina is attributed to the formation of an interfacial silica-alumina phase in between primary particles in an agglomerate and concluded that such an interfacial phase disrupts the γ-Al_2O_3 structure and improves thermal stability by retarding the α-Al_2O_3 formation. Therefore, H-MSA(x) is structurally stable because of the heightened presence of Al^V compared to MA and MSA(x).

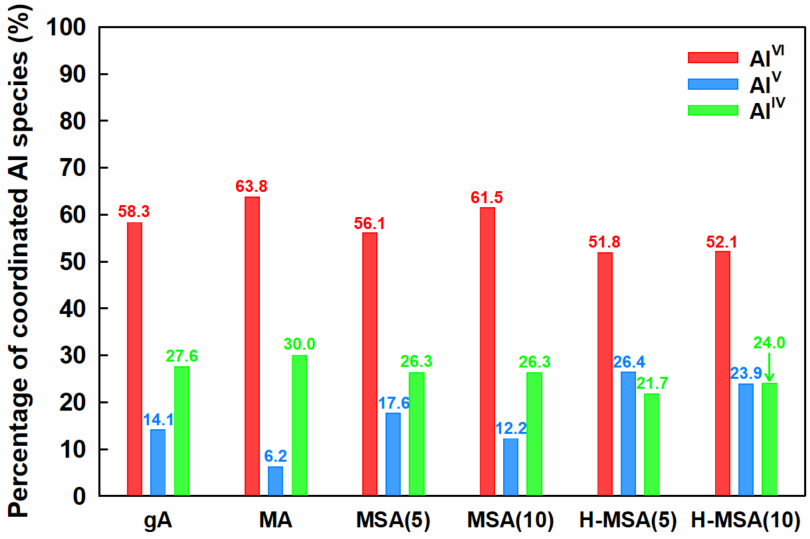

Figure 11. Composition of coordinated Al species (calculated by deconvolution of ^{27}Al MAS NMR spectra in Figure S6) for gA, MA, MSA(5), MSA(10), H-MSA(5), and H-MSA(10).

Additionally, it was reported that the increased concentration of Al^V could stabilize active PdO_x species and strongly interact with adjacent PdO_x on the surface of Pd particles [34]. This suggests that PdO_x/H-MSA(5) is capable of showing good and stable methane combustion performance owing to the heightened presence of Al^V and water tolerance, which are derived from the SDP method using TEOOS as a silane source.

3. Materials and Methods

3.1. Catalyst Preparation

The supporting MA (mesoporous alumina), MSA(x) (mesoporous silica-alumina), and H-MSA(x) (water-tolerant mesoporous silica-alumina) were prepared by the SDP (solvent deficient precipitation) method. For the synthesis of MA, 10.21 g AIP (aluminum isopropoxide, Sigma Aldrich, Munich, Germany) was mixed with 5.4 g water (equivalent to 6 mole of H_2O per AIP) in a mortar with a pestle at room temperature for 20 min. During this course, the mixture was changed from wet powder to liquid form and finally to paste state. The obtained paste was calcined at 800 °C for 5 h in a muffle furnace. The same procedure was used for the preparation of MSA and H-MSA, except the addition of TEOS (tetraethyl orthosillicate, Sigma Aldrich, Munich, Germany) and TEOOS (triethoxy(octyl)silane, Sigma Aldrich, Munich, Germany) for substitution of 5, 10, and 20 mol% AIP, respectively. Additionally, gA (γ-alumina) was purchased from STREM Chemicals. To the prepared supports, Pd of 2 wt% was loaded by incipient wetness impregnation using a solution of 10 wt% $4NH_3{\cdot}Pd(NO_3)_2$ in H_2O (Sigma Aldrich, Munich, Germany). Finally, the catalysts were dried at 105 °C for 12 h and calcined 600 °C for 5 h in the muffle furnace. Prior to activity tests, the calcined sample was sieved to between 200 and 300 μm mesh, because this size was examined in preliminary tests to be small enough to prevent internal mass transfer limitation.

3.2. Activity Test for Methane Combustion

Prior to the activity test, the calcined samples were subjected to methane activation using a gas of 20% CH_4 in N_2 balance (40 cm^3 min^{-1}). According to the report of Su et al., nucleated reduction happens when CH_4 rather than H_2 is used for activation of PdO [35]. In our preliminary studies, PdO on the MA were reduced by CH_4 in the temperature range 400–550 °C [36] and the catalyst activated with CH_4 at 600 °C showed a better performance than the one pretreated with air. In this work, the methane activation temperature was tuned to 500 °C because a higher fraction of PdO (34.7%) was formed in comparison with methane activation at 600 °C (27.8%), as shown in Figure S8. Thus, methane activation at 500 °C for 30 min was chosen to yield active PdO_x species.

A catalyst sample (60 mg) was activated in a quartz fixed bed reactor (outer diameter: 12 mm, inner diameter: 10 mm). After the reactor was cooled to 25 °C, the flow was switched to a reaction gas mixture of 4000 ppm CH_4, 12% O_2 and 5% H_2O in N_2 balance at a total flow rate of 200 cm^3 min^{-1} (corresponding to GHSV of 200,000 cm^3 $g_{cat}{}^{-1}$ h^{-1}). Then, the reactor was heated to 600 °C at a ramping rate of 5 °C min^{-1}, followed by cooling to 25 °C in a flow of reaction gas mixture. This procedure was repeated to examine catalyst stability. Additionally, isothermal tests were conducted at 500 °C with the same gas mixture as above. The concentrations of methane at the inlet ($CH_{4,in}$) and outlet ($CH_{4,out}$) were measured using an infrared gas analyzer (Fuji Electric Corp., Tokyo, Japan). Methane conversion was calculated using the following equation: methane conversion (%) = ($CH_{4,in}$ − $CH_{4,out}$)/$CH_{4,in}$ × 100.

3.3. Characterization

X-ray diffraction analysis was conducted with a Rigaku MiniFlex600 (Rigaku Corp., Tokyo, Japan) using a Cu Kα radiation at 40 kV and 15 mA to identify the crystalline structures of supports and catalysts in 2θ range from 10° to 80° at a scan speed of 10° min^{-1} with a step of 0.02°.

The specific Brunauer-Emmett-Teller surface areas, total pore volumes and average pore diameters of catalysts (100 mg) were measured at 77 K in a Micromeritics 3Flex (Micromeritics Instrument Corp., Norcross, GA, USA) after samples were degassed at 150 °C for 1 h for removing adsorbed chemicals.

The actual Pd loading was measured with an inductively coupled plasma optical emission spectrometer (ICP-OES) using a Thermo Scientific iCAP 7000 (Thermo Fisher Scientific Corp., Waltham, MA, USA), after a sample dissolved in a mixture of HNO_3 and HCl (1:6, *v*/*v*) was pretreated in a Milestone Ethos Easy Microwave digestion system. The carbon content was determined by elemental analysis using a Thermo Scientific Flash EA 1112 (Thermo Fisher Scientific Corp., Waltham, MA, USA). Thermogravimetric analysis was conducted in a NETZSCH TG209F1 (Erich NETZSCH GmbH & Co. Holding KG, Selb, Germany). The sample (30 mg) was heated to 900 °C at a rate of 10 °C min^{-1} in an air flow (100 cm^3 min^{-1}).

X-ray photoelectron spectroscopy analysis was conducted using a Thermo Scientific K-alpha plus spectrometer (Thermo Fisher Scientific Corp., Waltham, MA, USA) with a monochromatic Al Kα X-ray source operated at a voltage of 1486.6 eV. All spectra were collected with a step of 0.1 eV and a pass energy of 50 eV using the C 1s binding energy of 284.6 eV for calibration.

To investigate the Pd dispersion and Pd particle size, CO-chemisorption analysis was carried out using a BELCAT-B instrument (MicrotracBEL Corp., Osaka, Japan). Prior to the analysis, the sample (50 mg) was reduced at 350 °C for 1 h at a ramping rate of 5 °C min^{-1} in 30 cm^3 min^{-1} of 10% H_2/Ar and then purged for 30 min in a He flow. After this reduction, the sample was cooled down to 35 °C in He atmosphere and 5% CO/He gas was repeatedly injected as pulse (volume of sample loop: 0.994 cm^3) until the sample was saturated. The Pd dispersion and Pd particle size were calculated from CO uptake data, under the assumption that Pd crystallite is spherical and the ratio of adsorbed CO to Pd is 1.

H_2 temperature-programmed reduction measurement was performed in a Micromeritics AutoChem 2910 (Micromeritics Instrument Corp., Norcross, GA, USA). After the calcined sample (200 mg) was pretreated at 500 °C for 1 h in He, it was cooled to 50 °C. Then, 10% H_2/Ar was fed at a rate of 50 cm^3 min^{-1}, followed by heating to 350 °C at a rate of 5 °C min^{-1}.

Fourier-transform infrared spectra were obtained in a Thermo Fisher Scientific Nicolet 6700 (Thermo Fisher Scientific Corp., Waltham, MA, USA) to figure out the presence of C–H stretching in the range 3000–2800 cm^{-1}. Before FT-IR analysis, a KBr (Sigma Aldrich, Munich, Germany) pellet of the mixed powder (KBr 98 mg, sample 2 mg) was prepared, and then that pellet was installed to record the spectra.

Attenuated total reflectance infrared spectra were collected in a Nicolet iS50 (Thermo Fisher Scientific Corp., Waltham, MA, USA) to access the extent of water uptake after thermal pretreatment of a powder sample (50 mg) was conducted in different manners with a tube reactor. All spectra were recorded in the range 4000–400 cm^{-1} with 32 scans and a resolution of 4 cm^{-1}, where KBr (Sigma Aldrich, Munich, Germany) was used for a background spectrum.

FT-IR spectroscopy with pyridine adsorption was conducted in the same instrument equipped with MCT-A detector for calculation of Lewis and Brønsted acid sites of all supports. The probe molecule was adsorbed inside a Specac HTHP cell (Specac Ltd., Orpington, Kent, England). A sample pellet (30 mg) was pretreated at 300 °C for 1 h under vacuum (10^{-3} mbar) and the probe molecule pyridine (5 μL) was then directly injected after cooling down to 150 °C. Following the degassing at 150 °C for 30 min, IR spectra were acquired with 32 scans and a resolution of 4 cm^{-1}.

Solid-state ^{27}Al magic angle spinning nuclear magnetic resonance spectra were recorded with an Advance III HD (Bruker Corp., Billerica, MA, USA) using a 4 mm broadband MAS probe. The NMR frequency was 130.3 MHz and the chemical shift was referenced to 1 M $AlCl_3$(*aq*) as 0.0 ppm. The sample was packed in a 4 mm diameter rotor and spun at 10 kHz. The spectra were acquired by Fourier transform of the free induction decay signals with a single 1.0 μs pulse, resulting in a flip angle of about $\pi/12$ and a recycle delay time of 1 s. The measurements were performed with 1024 scans.

For wettability experiments, a sample (ca. 100 mg) was pelletized at 5.0 tons for 1 min using a CrushIR Digital Hydraulic Press (PIKE, Madison, WI, USA). Then, two droplets of water were added onto each pelletized disc followed by measurement of contact angle.

4. Conclusions

For methane combustion, we demonstrated the advantage of water-tolerant mesoporous silica-alumina prepared by the SDP method using TEOOS and AIP as Si and Al sources, respectively. Compared to the other reference supports, the H-MSA(*x*) exhibited better textural properties, leading to higher dispersion of PdO_x, and water tolerance provided by the silica present on the external particle surface. It also contained more penta-coordinated Al species and weak Lewis acidity, contributing to stabilization of active PdO_x phase and reduction of water-poisoning effect, respectively. The repeated temperature-programmed cycles and isothermal tests in the presence of water vapor revealed the superior stability of PdO_x/H-MSA(5) to the other prepared catalysts: the methane conversion over PdO_x/H-MSA(5) showed a very small decrease from 99.8% to 97.8% at 500 °C for 24 h. Consequently, it is believed that the H-MSA would be a suitable support for stable performance of PdO_x in methane combustion under exhaust gas conditions.

Supplementary Materials: The following are available online at https://www.mdpi.com/article/10.3390/catal11060670/s1, Figure S1: FT-IR spectra of the as-synthesized samples (H-MSA(10), MSA(10), MA and gA) and water-tolerant γ-alumina (H-gA), Figure S2: Wettability experiments with H-MSA(10), MSA(10), MA, and gA. The measured contact angle is added into each panel except MA showing the spreading behavior, Figure S3: N_2 adsorption-desorption isotherms of the prepared support materials, Figure S4: Pore size distribution curves of the prepared support materials: (a) MA and (b) gA, Figure S5: TEM images of (a) the fresh PdO_x/H-MSA(10), (b) spent

PdO_x/H-MSA(10), (c) fresh PdO_x/MSA(10), and (d) spent PdO_x/MSA(10). The spent samples were obtained after isothermal test at 500 °C for 24 h. Insets represent the particle size distribution of PdO_x determined by statistical analysis of ca. 30–40 white particles, Figure S6: XPS results of (a) H-MSA(*x*) and (b) MSA(*x*) in the binding energy region of Si 2p, Figure S7: ^{27}Al MAS NMR spectra of all supports: (a) H-MSA(5), (b) H-MSA(10), (c) MSA(5), (d) MSA(10), (e) MA and (f) gA (red: octahedral Al^{VI}; blue: penta-coordinated Al^{V}; green: tetrahedral Al^{IV}). The fitting results are marked by gray dots, Figure S8: XPS spectra of the catalyst samples pretreated with 20% CH_4 in N_2 at 500 and 600 °C, Table S1: Isothermal methane combustion performance of the reported Pd catalysts and PdO_x/H-MSA(5) in this work.

Author Contributions: Data curation, M.K. and S.L.; conceptualization, M.K., C.-H.S., J.H.B. and Y.-W.S.; methodology, M.K. and S.L.; validation, M.K., S.L. and C.K.; investigation, M.K., S.L. and C.K. (M.K.: material design, synthesis, and catalyst characterization, S.L.: catalyst characterization and catalytic experiments, C.K.: catalytic experiments); visualization, M.K. and Y.-W.S.; supervision, Y.-W.S.; writing—original draft preparation, M.K.; writing—review and editing, M.K. and Y.-W.S.; project administration, Y.-W.S.; funding acquisition, Y.-W.S. All authors have read and agreed to the published version of the manuscript.

Funding: This research was funded by the Basic Science Research Program through the National Research Foundation of Korea, grant number NRF-2016R1A6A1A03013422 under the Ministry of Education, Republic of Korea. The APC was funded by the Basic Science Research Program through the National Research Foundation of Korea, grant number NRF-2016R1A6A1A03013422 under the Ministry of Education, Republic of Korea.

Acknowledgments: The authors thank LINC+ Analytical Equipment Center at Hanyang University for help of catalyst characterization works.

Conflicts of Interest: The authors declare no conflict of interest.

References

1. Mihai, O.; Smedler, G.; Nylén, U.; Olofsson, M.; Olsson, L. The effect of water on methane oxidation over Pd/Al_2O_3 under lean, stoichiometric and rich conditions. *Catal. Sci. Technol.* **2017**, *7*, 3084–3096. [CrossRef]
2. Nilsson, J.; Carlsson, P.-A.; Martin, N.M.; Adams, E.C.; Agostini, G.; Grönbek, H.; Skoglundh, M. Methane oxidation over Pd/Al_2O_3 under rich/lean cycling followed by operando XAFS and modulation excitation spectroscopy. *J. Catal.* **2017**, *356*, 237–245. [CrossRef]
3. Baylet, A.; Marecot, P.; Duprez, D.; Castellazzi, P.; Groppi, G.; Forzatti, P. In situ Raman and in situ XRD analysis of PdO reduction and Pd^0 oxidation supported on γ-Al_2O_3 catalyst under different atmospheres. *PCCP* **2011**, *13*, 4607–4613. [CrossRef] [PubMed]
4. Ciuparu, D.; Lyubovsky, M.R.; Altman, E.; Pfefferle, L.D.; Datye, A. Catalytic combustion of methane over palladium-based catalysts. *Catal. Rev.* **2002**, *44*, 593–649. [CrossRef]
5. McCarty, J.G. Kinetics of PdO combustion catalysis. *Catal. Today* **1995**, *26*, 283–293. [CrossRef]
6. Oh, S.H.; Mitchell, P.J.; Siewert, R.M. Methane oxidation over alumina-supported noble metal catalysts with and without cerium additives. *J. Catal.* **1991**, *132*, 287–301. [CrossRef]
7. Baldwin, T.R.; Burch, R. Catalytic combustion of methane over supported palladium catalysts: I. Alumina supported catalysts. *Appl. Catal.* **1990**, *66*, 337–358.
8. Liu, Y.; Wang, S.; Gao, D.; Sun, T.; Zhang, C.; Wang, S. Influence of metal oxides on the performance of Pd/Al_2O_3 catalysts for methane combustion under lean-fuel conditions. *Fuel Process. Technol.* **2013**, *111*, 55–61. [CrossRef]
9. Lott, P.; Dolcet, P.; Casapu, M.; Grunwaldt, J.-D.; Deutschmann, O. The effect of prereduction on the performance of Pd/Al_2O_3 and Pd/CeO_2 catalysts during methane oxidation. *Ind. Eng. Chem. Res.* **2019**, *58*, 12561–12570. [CrossRef]
10. Losch, P.; Huang, W.; Vozniuk, O.; Goodman, E.D.; Schmidt, W.; Cargnello, M. Modular Pd/zeolite composites demonstrating the key role of support hydrophobic/hydrophilic character in methane catalytic combustion. *ACS. Catal.* **2019**, *9*, 4742–4753. [CrossRef]
11. Burch, R.; Urbano, F.J.; Loader, P.K. Methane combustion over palladium catalysts: The effect of carbon dioxide and water on activity. *Appl. Catal. A* **1995**, *123*, 173–184. [CrossRef]
12. Roth, D.; Gélin, P.; Primet, M.; Tena, E. Catalytic behaviour of Cl-free and Cl-containing Pd/Al_2O_3 catalysts in the total oxidation of methane at low temperature. *Appl. Catal. A* **2000**, *203*, 37–45. [CrossRef]
13. Schwartz, W.R.; Ciuparu, D.; Pfefferle, L.D. Combustion of methane over palladium-based catalysts: Catalytic deactivation and role of the support. *J. Phys. Chem. C* **2012**, *116*, 8587–8593. [CrossRef]
14. Barrett, W.; Shen, J.; Hu, Y.; Hayes, R.E.; Scott, R.W.J.; Semagina, N. Understanding the role of SnO_2 support in water-tolerant methane combustion: In situ observation of $Pd(OH)_2$ and comparison with Pd/Al_2O_3. *ChemCatChem* **2019**, *11*, 1–10.

15. Cargnello, M.; Jaén, J.J.D.; Garrido, J.C.H.; Bakhmutsky, K.; Montini, T.; Gámez, J.J.C.; Gorte, R.J.; Fornasiero, P. Exceptional activity for methane combustion over modular Pd@CeO_2 subunits on functionalized Al_2O_3. *Science* **2012**, *337*, 713–717. [CrossRef]
16. Smith, S.J.; Huang, B.; Liu, S.; Liu, Q.; Olsen, R.E.; Boerio-Goates, J.; Woodfield, B.F. Synthesis of metal oxide nanoparticles via a robust "solvent-defient" method. *Nanoscale* **2015**, *7*, 144–156. [CrossRef]
17. Huang, B.; Bartholomew, C.H.; Woodfield, B.F. Facile structure-controlled synthesis of mesoporous γ-alumina: Effects of alcohols in precursor formation and calcination. *Micropor. Mesopor. Mater.* **2013**, *177*, 37–46. [CrossRef]
18. Huang, B.; Bartholomew, C.H.; Smith, S.J.; Woodfield, B.F. Facile solvent-deficient synthesis of mesoporous γ-alumina with controlled pore structures. *Micropor. Mesopor. Mater.* **2013**, *165*, 70–78. [CrossRef]
19. Mardkhe, M.K.; Huang, B.; Bartholomew, C.H.; Alam, T.M.; Woodfield, B.F. Synthesis and characterization of silica doped alumina catalyst support with superior thermal stability and unique pore properties. *J. Porous. Mater.* **2016**, *23*, 475–487. [CrossRef]
20. Hong, E.; Kim, C.; Lim, D.-H.; Cho, H.-J.; Shin, C.-H. Catalytic methane combustion over Pd/ZrO_2 catalysts: Effect of crystalline structure and textural properties. *Appl. Catal. B* **2018**, *232*, 544–552. [CrossRef]
21. Rytter, E.; Tsakoumis, N.E.; Myrstad, R.; Yang, J.; Lögdberg, S.; Holmen, A.; Rønning, M. Hydrophobic catalyst support surfaces by silylation of γ-alumina for Co/Re Fischer-Tropsch synthesis. *Catal. Today* **2018**, *299*, 20–27. [CrossRef]
22. Al-Abadleh, H.A.; Grassian, V.H. FT-IR study of water adsorption on aluminum oxide surfaces. *Langmuir* **2003**, *19*, 341–347. [CrossRef]
23. Zheng, Q.; Farrauto, R.; Deeba, M. Part II: Oxidative thermal aging of Pd/Al_2O_3 and Pd/Ce_xO_y-ZrO_2 in automotive three way catalysts: The effects of fuel shutoff and attempted fuel rich regeneration. *Catalysts* **2015**, *5*, 1797–1814. [CrossRef]
24. Oh, J.; Bathula, H.B.; Park, J.H.; Suh, Y.-W. A sustainable mesoporous palladium-alumina catalyst for efficient hydrogen release from N-heterocyclic liquid organic hydrogen carriers. *Commun. Chem.* **2019**, *2*, 68. [CrossRef]
25. Esteves, L.M.; Brijaldo, M.H.; Passos, F.B. Decomposition of acetic acid for hydrogen production over Pd/Al_2O_3 and Pd/TiO_2: Influence of metal precursor. *J. Mol. Catal. A* **2016**, *422*, 275–288. [CrossRef]
26. Bhogeswararao, S.; Srinivas, D. Catalytic conversion of furfural to industrial chemical over supported Pt and Pd catalysts. *J. Catal.* **2015**, *327*, 65–77. [CrossRef]
27. Murata, K.; Mahara, Y.; Ohyama, J.; Yamamoto, Y.; Arai, S.; Satsuma, A. The metal-support interaction concerning the particle size effect of Pd/Al_2O_3 on methane combustion. *Angew. Chem. Int. Ed.* **2017**, *56*, 15993–15997. [CrossRef]
28. Chen, J.; Zhong, J.; Wu, Y.; Qu, P.; Xiao, X.; Zhang, G.; Liu, X.; Jiao, Y.; Zhong, L.; Chen, Y. Particle size effects in stoichiometric methane combustion: Structure−activity relationship of Pd catalyst supported on gamma-alumina. *ACS Catal.* **2020**, *10*, 10339–10349. [CrossRef]
29. Toso, A.; Colussi, S.; Llorca, J.; Trovarelli, A. The dynamics of PdO-Pd phase transfromation in the presnece of water over Si-doped Pd/CeO_2 methane oxidation catalysts. *Appl Catal. A* **2019**, *574*, 79–86. [CrossRef]
30. Toso, A.; Colussi, S.; Padigapaty, S.; de Leitenburg, C.; Trovarelli, A. High stability and activity of solution combustion synthesized Pd-based catalysts for methane combustion in presence of water. *Appl. Catal. A* **2018**, *230*, 237–245. [CrossRef]
31. Kim, C.; Hong, E.; Shin, C.-H. Improvement of methane combustion activity for Pd/ZrO_2 catalyst by simple reduction/reoxidation treatment. *Catalysts* **2019**, *9*, 838. [CrossRef]
32. Emeis, C.A. Determination of integrated molar extinction coefficients for infrared absorption bands of pyridine adsorbed on solid acid catalysts. *J. Catal.* **1993**, *141*, 347–354. [CrossRef]
33. Dong, Y.; Huang, S.; Wang, S.; Zhao, Y.; Gong, J.; Ma, X. Synthesis of dimethyl carbonate through vapor-phase carbonylation catalyzed by Pd-doped zeolites: Interaction of Lewis acidic sites and Pd species. *ChemCatChem* **2013**, *5*, 2174–2177. [CrossRef]
34. Duan, H.; You, R.; Xu, S.; Li, Z.; Qian, K.; Cao, T.; Huang, W.; Bao, X. Pentacoordinated Al^{3+}-stabilized active Pd structure on Al_2O_3-coated palladium catalysts for methane combustion. *Angew. Chem. Int. Ed.* **2019**, *58*, 12043–12048. [CrossRef] [PubMed]
35. Su, S.C.; Carstens, J.N.; Bell, A.T. A study of the dynamics of Pd oxidation and PdO reduction by H2 and CH4. *J. Catal.* **1998**, *176*, 125–135. [CrossRef]
36. Kim, M.; Lim, S.; Bathula, H.B.; Heo, I.; Kim, J.-R.; Lee, J.H.; Suh, Y.-W. Methane combustion over Pd catalysts supported on mesoporous alumina. *KSAE* **2020**, *28*, 353–357. [CrossRef]